Journal of The Electrochemical
Society

Three-Dimensional Coating Layer Modified Polyolefin Ceramic-Coated Separators to Enhance the Safety Performance of Lithium-Ion Batteries

To cite this article: Longqing Peng *et al* 2019 *J. Electrochem. Soc.* **166** A2111

Journal of The Electrochemical Society, **166** (10) A2111-A2120 (2019)
0013-4651/2019/166(10)/A2111/10/$38.00 © The Electrochemical Society

Three-Dimensional Coating Layer Modified Polyolefin Ceramic-Coated Separators to Enhance the Safety Performance of Lithium-Ion Batteries

Longqing Peng,[1] Xiu Shen,[1] Jianhui Dai,[1] Xin Wang,[1] Jing Zeng,[1] Boyang Huang,[1] Hang Li,[2] Peng Zhang,[2,z] and Jinbao Zhao [1,2,*,z]

[1] *College of Chemistry and Chemical Engineering, Xiamen University, Engineering Research Center of Electrochemical Technology, Ministry of Education, State-Province Joint Engineering Laboratory of Power Source Technology for New Energy Vehicle, Xiamen 361005, China*
[2] *College of Energy Research & School of Energy Research, Xiamen University, Xiamen 361102, China*

Although the ceramic-coated separators have been industrialized and widely used in power lithium-ion batteries to replace the polyolefin separators, the safety of batteries still cannot fully meet the demand of practical application with the rapid growth of energy density. In this work, a ceramic-coated separator further modified by phenol-formaldehyde resin has been developed, in which a three-dimension coating layer is formed both on the surface and in the pores of the pristine separator by introducing phenol-formaldehyde resin through a simple soakage process. Such membranes show extremely high thermal stability up to 300°C, maintain a high mechanical strength even after a heat-treatment at 220°C for 30 min, and show a shut-down function above 138°C. With the advantages of abundant sources, low cost, environment-friendly property and simple preparation process, the phenol-formaldehyde resin modified separators are expected to replace the commercial ceramic-coated separators, greatly improve the safety performance of batteries, and realize the reassuring application of lithium-ion batteries in power batteries and large-scale energy storage devices.
[DOI: 10.1149/2.1141910jes]

Manuscript submitted March 13, 2019; revised manuscript received June 10, 2019. Published June 18, 2019.

In recent years, electric vehicles (EVs) have been developed rapidly for its environment-friendly property without emission of harmful vehicle exhaust, meanwhile the lithium-ion batteries (LIBs) are regarded as the most competitive power source due to their high mass energy density and long cycle life.[1,2] However, frequent battery explosion accidents have also severely hit the enthusiasm of consumers, and restricted the application of power LIBs in EVs. Therefore, it is urgent to improve the safety to meet higher requirements of LIBs with continuously increasing energy density.

The separator plays a crucial role in the LIBs. On one hand, it acts as a barrier to prevent the direct contact of electrodes and infiltration of materials particles, but on the other hand, it shall maintain conductive channel to permit the transportation of Li^+ ions in electrolyte.[3,4] At present, porous polyolefin membrane is mostly used as the separators of LIBs for its satisfactory electrochemical stability, mechanical strength and low cost. However, the thermal stability of polyolefin membrane is quite poor, and it will show a large dimension shrinkage at elevated temperature, leading to an internal short circuit of batteries, which may finally result in a fire or even an explosion.[1,5–7]

Many measures have been tried to overcome this problem, and it is clear that the most effective strategy is to enhance the thermal stability of the separator. Based on this point, one strategy is to prepare porous membranes with high temperature resistant polymer matrix such as polyimide (PI).[8,9] However, it is hard to achieve commercial application since its high cost, poor mechanical strength and non-environment friendly manufacture process using harmful organic solvents. The other method is to utilize solid electrolytes with both inorganic and polymer based materials,[10–13] but the low ionic conductivity and high interface impedance limit their application in the LIBs. Nowadays, the most practicable way could be modifying commercial polyolefin separators with a thin coating layer of inorganic ceramic particles, named ceramic-coated separators (CCS), which have already achieved commercial production and used in the EVs recently.[14–18] It not only remains the strong mechanical strength of polyolefin separators, but also improves the thermal stability and wettability by coating inorganic ceramic particles. However, the thermal stability improvement of CCS is still not effective enough since the poor mechanical strength of ceramic layer and the weak bonding forces between the polyolefin matrix and ceramic particles will make the ceramic layer fracture and even pill off from polyolefin separator at elevated temperature, losing the protection function of ceramic layer.[16,18]

In order to further improve the thermal stability of the CCS, we have developed a modified CCS by introducing high temperature resistance polymer to form a three-dimension coating layer throughout the entire pristine CCS membranes. The three-dimension coating layer can connect ceramic layer with polyolefin membrane substrate as a whole, which not only enhances the mechanical strength of ceramic layer, preventing it from crashing with the shrinking of polyolefin membrane, but also improves the adhesion between ceramic layer and polyolefin separator, averting the exfoliation of ceramic layer. Herein, phenol-formaldehyde resin (PFR) was chosen as the high temperature resistance polymer modification material. As schematically demonstrated in Figure 1, PFR can infiltrate through separator by a quick soakage process, and after a subsequent cure process, via dehydration condensation, PFR can form a highly cross-linked three-dimensional coating layer both on the ceramic layer and the microporous surface of PE layer, which makes the ceramic layer integrate with PE layer and could further improve the thermal stability and mechanical strength of the whole separator.[19]

PFR is chosen as the modification material based on the following consideration: 1) PFR has been widely used in electrical equipment and fire prevention materials because of its good insulating property, dimensional stability and heat resistance.[20,21] 2) Low molecular weight PFR oligomer is small enough to permeate into the dozens nanometers pores of separators, and then, after a simple thermal curing process at a relatively low temperature, it will form a cross-linked macromolecule three-dimension coating layer throughout entire separators, which can further improve the thermal stability and mechanical strength of the whole separator. 3) The abundant source and low cost of PFR provide the solid foundation of practical application, and the preparation process is environment friendly. 4) Combining the inherent function of ceramic particles and further improved PFR modification components, the developed CCS@PFR has showed substantially enhanced performance, including the excellent mechanical strength of polyolefin separator, the wettability of inorganic ceramic particles, and the high temperature resistance of polymer. We choose commercial ceramic-coated separator as pristine separator, and as a result, the CCS@PFR is very easy to commercialize the production. Meanwhile, the battery with this CCS@PFR show almost no energy density decline and cost rise, which proves its practical application to replace the nowadays CCS and improves the safety of LIBs with continuously increased energy density.

---

*Electrochemical Society Member.
[z] E-mail: pengzhang@xmu.edu.cn; jbzhao@xmu.edu.cn

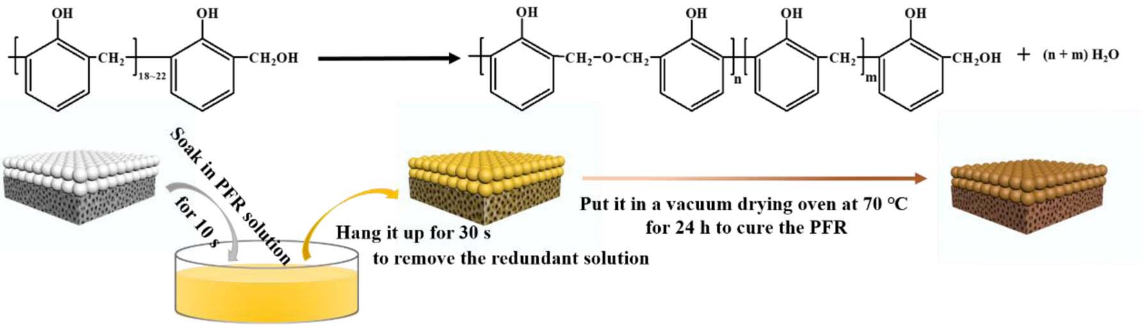

Figure 1. Schematic illustration of the preparation of the CCS@PFR.

Experimental

Preparation of the CCS@PFR.—The CCS@PFR was prepared by immersing the ceramic-coated separator (20 μm polyethylene (PE) substrate layer with 3 μm Al_2O_3 ceramic coating layer, Jinhuigaoke, Guangdong, China) into 50 $g{\cdot}L^{-1}$ PFR ($M_w = 2000$, Shanghai Macklin Biochemical Co., Ltd) solution with ethanol as the solvent for about 10 seconds, followed by hanging it up for around 30 seconds to remove the redundant solution, as schematically demonstrated in Figure 1. After dried in a vacuum oven at 70°C for 24 h to condense the PFR and remove the residual solvent, the CCS@PFR was obtained.

Electrode preparation and cell assembly.—The slurry containing 80 wt% $LiNi_{0.6}Co_{0.2}Mn_{0.2}O_2$, 10 wt% acetylene black, and 10 wt% polyvinylidene fluoride (PVDF) with the N-methyl-pyrrolidine (NMP) as the solvent, was coated on the aluminum foils to prepare the positive electrodes. The 2016-type coin half-cells were assembled for the tests of the batteries performances by sandwiching a separator between a $LiNi_{0.6}Co_{0.2}Mn_{0.2}O_2$ positive electrode and a lithium-metal negative electrode. The commercial LB-301 electrolyte containing 1 M $LiPF_6$ in ethylene carbonate (EC)/dimethyl carbonate (DMC) (1:1 in volume, Zhangjiagang Guotaihuarong New Chemical Materials Co., Ltd) was used for the batteries performance tests. The cells were assembled under an argon atmosphere in a glove box (M. Braun GmbH).

Characterization and measurements.—The cross-section and surface morphologies of the separators were measured by the field emission scanning electron microscopy (FE-SEM, S-4800, Hitachi, Japan). Fourier transform infrared spectroscopy (FT-IR, Nicolet IS5 spectrometer, Thermo Fisher Scientific Inc) was used to determine the chemical composition of the separators and PFR.

The thermal stability of the separators was tested by cutting the separators into 2 cm × 2 cm squares and measuring the dimensional change after a 30 minutes heat-treatment at various temperatures from 110°C to 300°C. Thermal shrinkage (Ts) of the separators was calculated according to the following equation:

$$Ts = \frac{S_0 - S}{S_0} \times 100\% \qquad [1]$$

where S_0 and S are the areas of the separators before and after the heat-treatment, respectively. The mechanical strength of the separators was measured by the universal material testing machine (UTM-4000, SUNS, Shenzhen) at a strain rate of 4 mm/min. Differential scanning calorimetry (DSC) measurements were evaluated using Model STA 449 instrument (NETZSCH Machinery and Instruments Co., Ltd) at a heating rate of 5°C per minute from 35°C to 500°C under nitrogen atmosphere. The electrolyte uptake (Eu) was obtained by measuring the original weight of the separators (W_0) and the weight of the separators absorbing the liquid electrolyte (W), and was calculated by the equation as follows:

$$Eu = \frac{W - W_0}{W_0} \times 100\% \qquad [2]$$

The porosity (P) of the separator was obtained by measuring the weight of the separators before and after the immersion into n-butanol for 10 minutes, and calculated using the equation as follows:

$$P = \frac{m - m_0}{\rho \times V} \times 100\% \qquad [3]$$

Where m_0 and m are the weight of the membranes before and after the immersion in the n-butanol, respectively, ρ means the density of the n-butanol, and V means the volume of the separator which can be calculated from the area and thickness. The electrolyte affinity property of the separators was tested using a contact angle goniometer (Powereach JC2000C1, Shanghai Zhongchen Digital Technique Equipment Co., Ltd), and the commercial LB-301 electrolyte was used as the test liquid. In order to measure the ionic conductivity of the separators, a blocking-type cell was fabricated by sandwiching an electrolyte-soaked separator between two stainless steel sheets, and the impedance data of the separators were then recorded using an electrochemical working station (AutoLab, Sino-Metrohm Technology Ltd) over the frequency range of 1 Hz to 100 kHz. The ionic conductivity (σ) of the separators was calculated using the equation:

$$\sigma = \frac{d}{(R_b \times A)} \qquad [4]$$

where d means the thickness of the separators, A denotes the area of the stainless steel sheets, and R_b means the bulk impedance of the separators, which was obtained by fitting the result of AC impedance. In order to investigate the shut-down function of the separators, the AC impedance measurement was carried out using an AutoLab working station with the temperature increment from 110°C to 220°C at the rate of $1°C{\cdot}min^{-1}$.

The linear sweep voltammetry (LSV) was carried out to determine the electrochemical stability from 3 V to 5.5 V at $1mV{\cdot}s^{-1}$, using stainless steel and Li foil as the working and counter electrodes, respectively. The cycle performance was tested using a battery testing system (LAND-V34, Wuhan LAND Electronics Co., Ltd) as the following steps: the cell was firstly charged to 4.3 V under a constant current of 0.5 C, maintained at 4.3 V until the current decreased to the 10% of the initial current, and then discharged to 3.0 V under a constant current of 0.5 C. The cells were discharged at various current densities (0.5 C, 1.0 C, 2.0 C, 5.0 C and 10 C), and charged at the same rate of 0.5 C to investigate the C-rate performance.

Results and Discussion

Morphology and characterization.—Figure 2a presents the photographic image of the CCS (left) and CCS@PFR (right). After a simple dip process in PFR solution and curing process, the color of CCS@PFR changes from white to primrose yellow, which implies the successful coating of PFR. The surface morphologies of the ceramic side of CCS and CCS@PFR are presented in Figures 2b–2e, and the PE side of CCS and CCS@PFR are presented in Figures 2f and 2g, respectively. After coating PFR, both ceramic and PE sides of the membrane keep their original homogeneous morphology, and hardly blocking off the pores

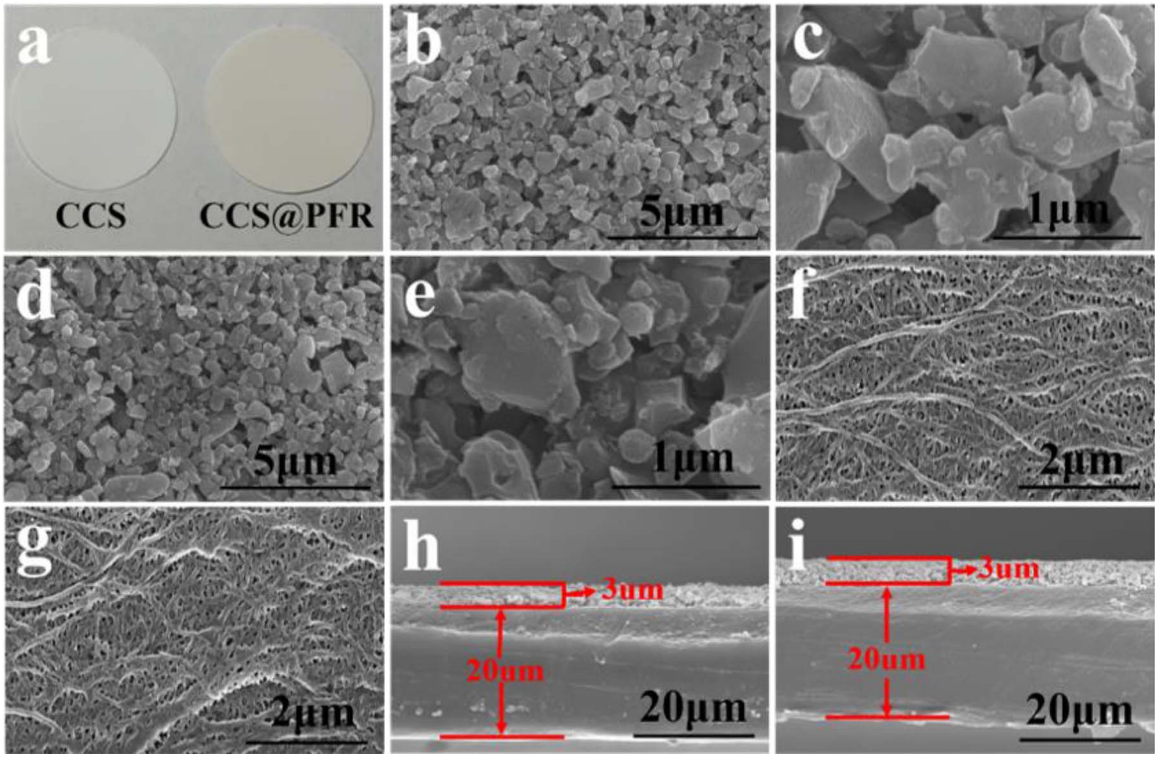

Figure 2. (a) The photos of CCS (left) and CCS@PFR (right). (b) SEM image and (c) enlarge image of ceramic side of CCS, (d) SEM image and (e) enlarge image of ceramic side of CCS@PFR, SEM images of PE side of (f) CCS and (g) CCS@PFR, SEM images of the cross-section of (h) CCS and (i) CCS@PFR.

in the porous separators, suggesting the thin PFR coating layer will not deteriorate the battery performance by plugging up the ion conduction channel in the battery. For further explanation, the cross-sectional morphologies of CCS and CCS@PFR membranes have been investigated, and the SEM images are shown in Figures 2h–2i. It can be seen that the thickness of PE layer is around 20 μm and the coating layer is approximately 3 μm for both membranes, demonstrating that the PFR modification layer scarcely changes the thickness of the pristine CCS membrane, and it is also beneficial to maintain the high energy density of LIBs. By measuring the weight of the separator before and after the PFR coating, the coating amount of the PFR is calculated to be 0.23 $mg \cdot cm^{-2}$, corresponding to only 11.8 wt% of CCS@PFR.

In order to further investigate the morphology of PFR inside the micro pores of the PE layer, we develop a tape-peeling strategy to examine the microporous structure inside the PE layer, since the polyolefin separator can't be quenched with liquid nitrogen and the microporous morphology will be easily destroyed by other mechanical cutting ways. As the cross-section morphology shown in Figure S1a, by peeling the separator with an adhesive tape, both the ceramic layer and the superficial PE can be peeled off, and the inner structure of PE layer would be possible to examine. The surface SEM images of the A spot (fracture point) and B spot (inside PE layer), as marked with red cycle in the schematic illustration inserted in Figure S1a, are shown in Figure S1b-1e. For the CCS, both the morphologies of A (Figure S1b) and B (Figure S1d) spots retain their original microporous morphologies, indicating the tape-peeling strategy is feasible to investigate the microporous morphology of inside PE layer. As for the CCS@PFR, both the morphologies of A (Figure S1c) and B (Figure S1e) spots have no visible change after the coating of PFR, which suggest that the PFR forms a very thin coating layer on the surface of micro pores inside the PE layer. Furthermore, the EDX element analysis is carried out at the B spot of CCS (B-CCS) and CCS@PFR (B-CCS@PFR), where the Al_2O_3 ceramic particles have been removed completely, so that the O element can be used to judge the existence of PFR. The EDX spectra results of B-CCS and B-CCS@PFR are shown in Figure S2a-2b, respectively. As shown, the B-CCS@PFR has a distinctly higher O element peak than B-CCS. In addition, the element analysis results of B-CCS and B-CCS@PFR are presented on Table S1 and Table S2 too, the average O element mass percentage of B-CCS is only 0.96%, which is negligible. Whereas, the average O element mass percentage of B-CCS@PFR is 5.31%, which verifies the existence of PFR in the PE layer.

To confirm the PFR modification layer on the pristine CCS membrane, the FT-IR of CCS, PFR and CCS@PFR has been carried out. As shown in Figure 3a, for the PFR, the peak at 3362 cm^{-1} is attributed to the phenolic-OH stretch vibration, the peak at 1610 cm^{-1} and 1510 cm^{-1} are attributed to the vibration of the aromatic ring in the PFR molecule structure, and the peak at 1441 cm^{-1} is attributed to the aliphatic C–H stretching.[22] The peak from 1170 cm^{-1} to 1300 cm^{-1} is attributed to the blending vibration of phenolic-OH.[23] For the CCS membrane, the peak at 3457 cm^{-1} is attributed to the hydroxyl groups on the surface of nano-Al_2O_3 particles, and the peak at 1460 cm^{-1} is owing to the -CH_2- bending vibration from PE separator substrate. While the peaks at 1736 cm^{-1}, 1251 cm^{-1}, and 1066 cm^{-1} are attributed to the carbonyl groups stretching vibration and C-O-C stretching vibration, which may derive from the esters binder in the ceramic coating layer. Moreover, it can be observed that there is a broad absorption band below 1000 cm^{-1} in the spectra, which is the characteristic of Al_2O_3.[24] After coating PFR, the CCS@PFR retains the peaks from pristine CCS still, including the peaks at 1736 cm^{-1}, 1251 cm^{-1}, 1066 cm^{-1} and the broad absorption band below 1000 cm^{-1}. However, several new peaks and shifts can be found. For example, the peaks at 1610 cm^{-1} and 1510 cm^{-1} originating from the aromatic ring stretch vibration of PFR, and the peak in the range from 1170 cm^{-1} to 1300 cm^{-1} deriving from the bending vibration of phenolic-OH appear after immersion in the PFR solution. It is notable that the peak switches from 3457 cm^{-1} to 3362 cm^{-1}, and the intensity of bands at 3700 ~ 3100 cm^{-1} and 1635 cm^{-1} diminish largely with negative peak at around 1635 cm^{-1} after coating PFR, which indicate the release of hydroxyl groups on the surface of nano-Al_2O_3 and phenolic hydroxyl group of PFR.[25] Therefore, the FT-IR spectra have proved the successful modification of PFR layer on CCS membrane

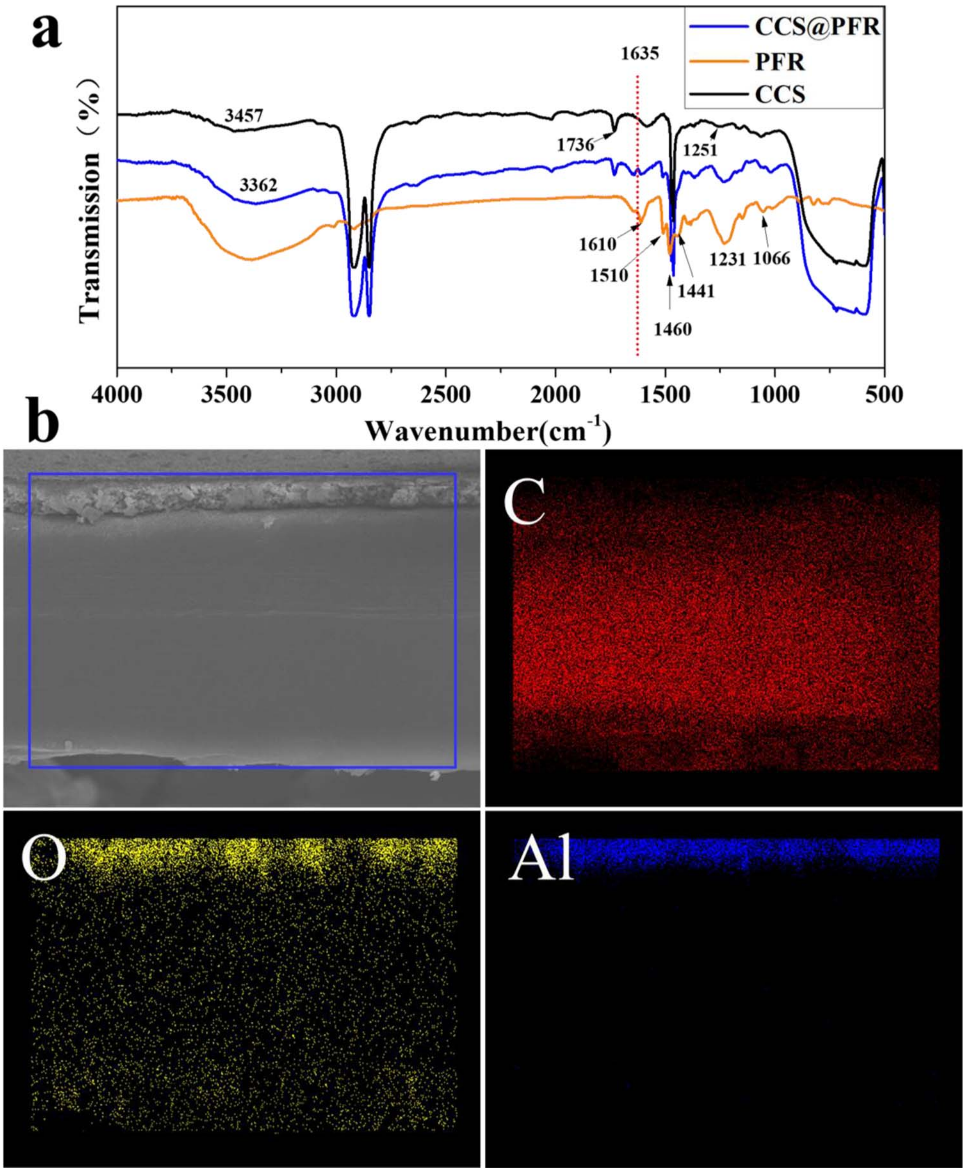

Figure 3. (a) The FT-IR spectra of CCS, CCS@PFR and PFR, (b) the SEM image of the cross-section of CCS@PFR and the elemental mapping of C, O, and Al.

and its strong adhesion to nano-Al_2O_3 particles on the pristine CCS membrane.

To further verify the existence of PFR both on the ceramic layer and PE layer, the ceramic layer and PE layer are divided apart to carry out FT-IR tests respectively. The FT-IR tests of ceramic layer are measured by scraping off the ceramic particles and tableting with KBr, and the FT-IR tests of PE layer are conducted by peeling off the ceramic layer and the superficial PE layer with adhesive tapes. The results of the FT-IR tests of the PE layer and ceramic layer are shown in Figure S3a and 3b, respectively. For the PE layer of CCS@PFR, the strong absorption band below 1000 cm^{-1} disappears, indicating the ceramic layer has been scraped off completely. Furthermore, many additional peaks, originating from PFR, can be observed at 3362 cm^{-1}, 1610 cm^{-1}, 1510 cm^{-1} and 1231 cm^{-1}, compared to the PE layer of CCS. As for the ceramic layer of CCS@PFR, the peak at 1231 cm^{-1} confirms the existence of PFR in the ceramic layer of CCS@PFR. Therefore, the FT-IR tests of the divided PE layer and ceramic layer further verifies the existence of PFR both on the ceramic layer and PE layer.

Moreover, the EDX element mapping analysis has been also conducted for the CCS@PFR cross-section to further ensure that the PFR modification takes place all around the ceramic coating layer and porous structure in the bulk of the PE layer. As shown in Figure 3b, there is an explicit boundary between the inorganic and polyolefin layer and the distribution of Al and C strictly corresponds to the area of the ceramic coating layer and the PE layer, respectively. However, the elemental O can be observed in both above layers, which verifies that the PFR not only modifies the surface of CCS membrane, but also permeates into the pores of the pristine separator. For comparison, the EDX element mapping analysis of CCS is shown in Figure S4. As shown, the distributions of Al and C strictly correspond to the area of the ceramic coating layer and the PE layer, respectively, which is similar to the CCS@PFR, while the distribution of O element is mainly present in the ceramic layer, hardly existing in the PE layer.

Therefore, it is obvious that a very thin three-dimension PFR coating layer has been infiltrated throughout the entire substrate separator by the simple dip and curing processes. The PFR coating layer is formed not only on the ceramic layer but also on the microporous surface of PE layer. As a result, it makes the ceramic layer integrate with PE separator and could further improve the thermal stability and mechanical strength of the whole separator.

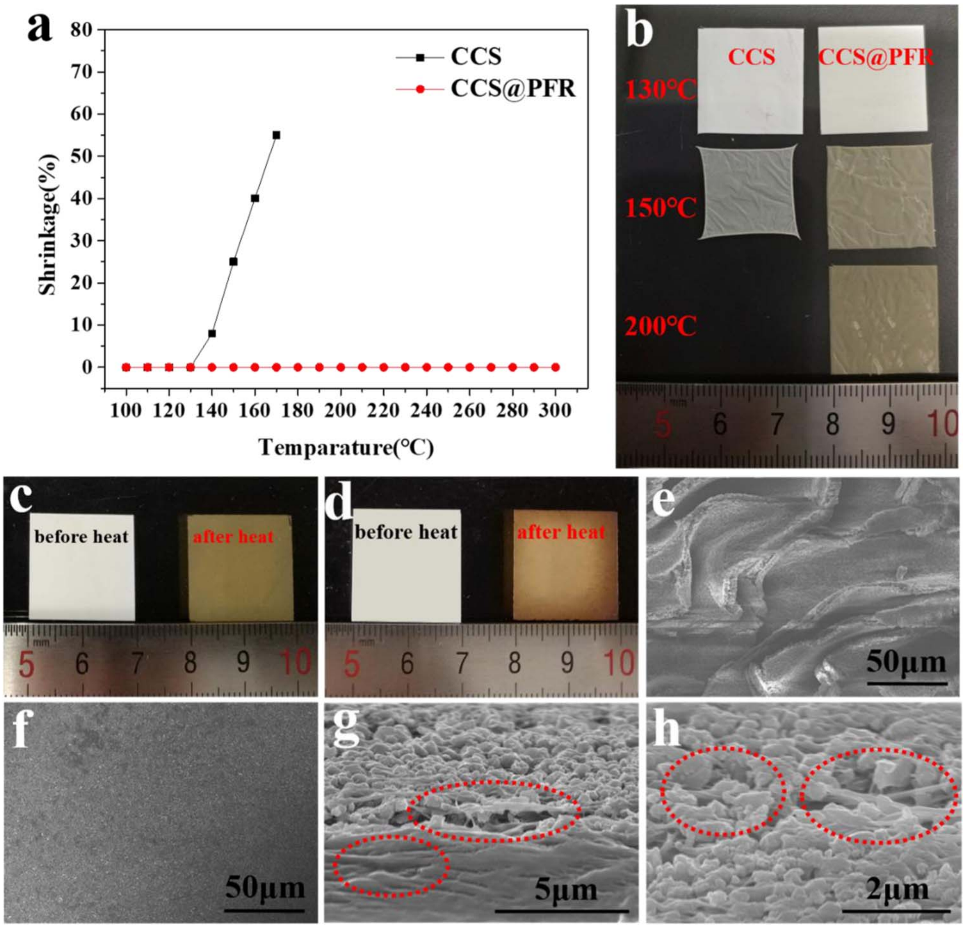

Figure 4. (a) The thermal shrinkage of the CCS and CCS@PFR as a function of temperature, (b) the images of CCS and CCS@PFR after a heat-treatment at 130°C, 150°C, and 200°C, the images of CCS@PFR before and after a heat-treatment at (c) 250°C and (d) 300°C, (e) the SEM images of CCS after a heat-treatment at 150°C, (f) the SEM images of CCS@PFR after a heat-treatment at 300°C, (g) and (h) the cross-section of CCS@PFR ceramic layer after a heat-treatment at 200°C.

Thermal dimensional stability.—The most primary function of a separator is hindering the contact of the cathode from anode electrodes, meanwhile permitting the ion conduction by infiltration of electrolyte. Therefore, under any condition, a separator must have both chemical and thermal stability as well as sufficient mechanical strength.[26,27] Otherwise, the electrodes may contact to each other and lead to an internal short circuit, and finally result in a fire or even an explosion with the accumulation of heat. However, the thermal stability of polyolefin separators is poor, leading to a large shrinkage at elevated temperature.[18] Moreover, the polyolefin separators will lose their mechanical strength along with the melting itself.[28] It has been proved that it is practically effective to coat with a thin ceramic particles layer on the surface of polyolefin membranes, and these CCS membranes have been widely used in the power LIBs.[14,28] However, frequent electric vehicle accidents indicate that it is still far away from meeting the safety requirement of LIBs, particularly in large-scale applications, such as the EVs, military industry and large-scale energy storage. The thermal shrinkage measurement results displayed in Figure 4a clearly show that the CCS membrane starts to shrink above 130°C, and has a shrinkage of 8.0%, 25.0%, 40.1%, 55.4% at 140°C, 150°C, 160°C, 170°C, respectively, and finally turns into powders at 180°C, whereas the CCS@PFR has no obvious shrinkage even up to 300°C. Figure 4b shows the pictures of CCS and CCS@PFR membranes after a heat-treatment at 130°C, 150°C and 200°C for 30 min. It can be seen from the photos that the pristine CCS has an obvious shrinkage at 150°C, while the CCS@PFR has no visible shrinkage. The Figures 4c–4d show the pictures of CCS@PFR before and after a heat-treatment at 250°C and 300°C, respectively. It can be clearly identified that even up to 300°C, the CCS@PFR membrane still keeps the dimensional stability without any shrinkage compared to the membrane before heat-treatment.

To further study the mechanism of thermal dimensional stability improved by PFR modification, some control experiments have been conducted. Firstly, the thermal performance of PE separator modified with PFR (PE@PFR) by the same soakage process is checked. As shown in Figure S5, PE@PFR membrane starts to shrink at 120°C, and has a shrinkage of 26.1%, 40.3%, 48.6%, and 57.3% at 130°C, 140°C, 150°C, and 160°C, respectively, which is better than pristine PE separators but not comparable to the CCS@PFR membrane. This result clearly shows that simple PFR modification will enhance the thermal stability of PE separator indeed, but the excellent thermal stability of CCS@PFR shall be owing to the synergistic effect of PFR together with ceramic particle. On one hand, the PFR modification improves the integrity and mechanical strength of ceramic coating layer, preventing ceramic layer from cracking with the shrinkage of PE separator. As the result of the FT-IR shown, the PFR modification further conjoins unconsolidated ceramic particles into an integrated ceramic layer, so that amends the morphology and mechanical strength of ceramic coating layer. On the other hand, the overall modification of PFR throughout the whole membrane to form a three-dimension coating layer makes the ceramic layer integrate with PE separator, which reduces the plane contraction force of PE separator at elevated temperature, increases the interaction force between ceramic layer and PE separator, and averts the ceramic layer peeling from the PE

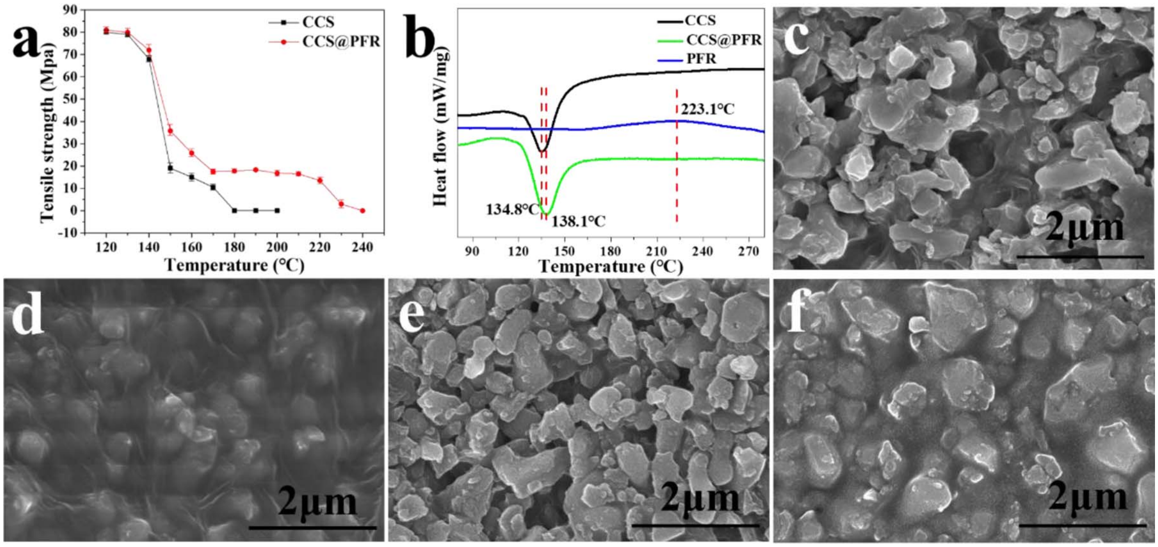

Figure 5. (a) Tensile strength of the CCS and CCS@PFR after a 30 min heat-treatment from 120°C to 240°C, (b) the DSC curve of CCS, CCS@PFR, and PFR after putting in a vacuum oven at 70°C for 24 h, the SEM image of CCS after a 30 min heat-treatment at (c) 170°C and (d) 180°C, the SEM image of CCS@PFR after a 30 min heat-treatment at (e) 220°C and (f) 230°C.

substrate separator. Secondly, the SEM exhibits that the morphology of commercial CCS membrane obviously shrinks after a heat-treatment. As shown in Figures 4e–4f, after a heat-treatment at 150°C, the ceramic layer of CCS membrane breaks up and peels from PE separator, while the CCS@PFR still keeps smoothly even up to 300°C. The cross-section SEM images of CCS@PFR ceramic layer after a heat-treatment at 200°C for 30 min are shown in Figures 4g–4h. It can be clearly identified that the three-dimensional PFR coating layer acts as a high temperature resistant holder throughout the entire separator, which enhances the strength of ceramic layer and the adhesion of ceramic layer to PE separator. Therefore, the CCS@PFR shows an excellent thermal dimension stability.

Thermomechanical strength.—The mechanical strength of membrane is also very significant for guaranteeing the safety of the LIBs. Although the polyolefin separators have excellent mechanical strength at room temperature, it degrades dramatically with the rise of temperature, which may lead to a short circuit as applied in the batteries. In order to study the effect of PFR modification on the mechanical properties of the CCS, the tensile strength tests have been carried out with the membranes before and after a heat-treatment from 130°C to 240°C for 30 min, respectively. As shown in Figure 5a, the tensile strength is improved largely after coating PFR, since the overall modified PFR makes ceramic layer integrate with PE separator, which enhances the mechanical strength of ceramic layer and prevents it from fracturing with PE separator. The first decline of both CCS and CCS@PFR starts above 130°C, and then with the rise of temperature, the mechanical strength of CCS gradually decreases until it pulverizes at 180°C, while CCS@PFR still maintains high mechanical strength until 220°C, and absolutely loses its strength at 230°C.

To further explain the role of phenolic resins in improving the mechanical properties of separators, the enlarged SEM images of CCS and CCS@PFR after heat treatments are shown in Figures 5c–5f. It can be seen that CCS retains its pristine morphology at 170°C, while the ceramic particles sink into the melted-down PE layer at 180°C, so that the CCS loses its integrity as well as the mechanical strength. The same phenomenon also can be seen on CCS@PFR from 220°C to 230°C. The DSC test has been also conducted to find out the reason of the decline of tensile strength. As shown in Figure 5b, the endothermic peaks of CCS and CCS@PFR at 134.8°C and 138.1°C, respectively, are due to the melt of PE polymer matrix, which are coincident with the first tensile strength decline of both CCS and CCS@PFR. It is worth noting that the melting point of CCS@PFR has a little lag due to the coating of PFR. Moreover, the exothermic peak of PFR at 223.1°C is attributed to the decomposition of PFR, according with the tensile strength decrease of the CCS@PFR at 230°C.

Shut-down function.—Shutdown function is a very effective way to guarantee the safety of LIBs,[4,9,29,30] which consists of low melt point part (LMPP), and high temperature resistance part (HTRP). The LMPP will melt at a low temperature and barrier the pores in the pristine separator to shut down the ionic conduction, and thus will prevent the exothermic side reaction from continuously taking place, while the HTRP will maintain dimensional stability and prevent direct contact between the electrodes. The synergistic effect of LMPP and HTRP makes cell possess shutdown function, which can prevent batteries from further thermal runaway at elevated temperature. As shown in Figure 6a, the PE separator melts and forms a densification layer at elevated temperature, blocking-up the free conduction of ions in the cell. The shutdown behavior of CCS and CCS@PFR was investigated by electrochemical impedance measurement with the temperature increasing from 90°C to 220°C at the rate of 1°C·min^{-1} as shown in Figure 6b. The CCS and CCS@PFR exhibit a sharp increase of the internal resistance at around 134°C and 138°C, respectively, which is owing to that the melt of PE substrate membrane blocks the pores of the substrate separator, and effectively obstructs the ionic transport between the cathode and anode. However, the impedance of CCS decreases to almost 0 Ω at 150°C, which implies that CCS suffers from an obvious dimensional change, leading to an internal short circuit in the cells. On the contrary, the AC impedance of CCS@PFR still keeps at the state of open circuit even above 220°C, which can actually prevents the battery from further thermal runaway at high temperature.

To further prove the above point of view, the SEM images of the PE side of CCS and CCS@PFR after a heat-treatment at 150°C are shown in Figures 6c–6d. The pores disappear with the melting of PE compared to the results at room temperature in Figure 2e, g. Furthermore, the image of separators after the shutdown function test is shown in Figure 6e. The CCS has a large shrinkage, while the CCS@PFR keeps the original size as the red circle denoted, which indicates that the CCS@PFR can assuredly maintain dimensional stability even in electrolyte at an elevated temperature, and block the contact between positive and negative electrodes, thus can ensure the safety of the batteries. The cross-section SEM images of CCS@PFR membrane after

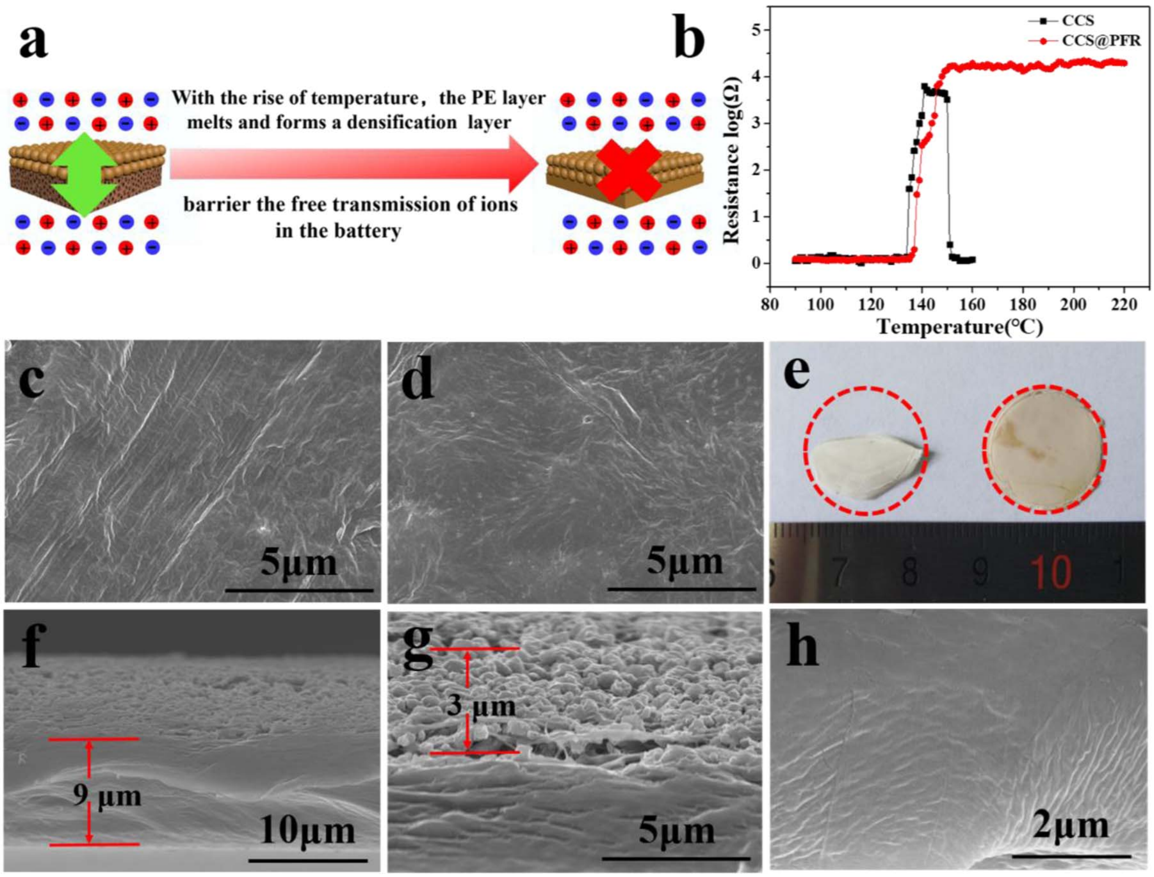

Figure 6. (a) Schematic illustration of the shut-down function of CCS@PFR, (b) the shutdown behavior of CCS and CCS@PFR, the SEM images of the PE side of (c) CCS and (d) CCS@PFR after a heat-treatment at 150°C, (e) the photo of CCS (left) and CCS@PFR (right) after the shutdown function test, (f-h) the cross-section SEM images of CCS@PFR after a heat-treatment at 200°C for 30 min.

a heat-treatment at 200°C for 30 minutes are also shown in Figures 6f–6h. It can be found that the thickness of PE layer declines from 20 μm to 9 μm, forming a more dense layer to block the ions conduction channel in the cell, while the ceramic layer still keeps its original thickness and morphology to block the contact between the electrodes, which exactly demonstrates the shutdown function of CCS@PFR.

Interfacial compatibility.—The interfacial compatibility is a crucial indicator for separators, since separators provide ion channel through infiltrating electrolyte. Due to the hydrophobic character, PE separators show a poor compatibility with conventional electrolyte. The contact angles of CCS and CCS@PFR were measured to investigate the interfacial compatibility of separators with conventional liquid electrolyte, and the PE separators, the same as the substrate of CCS, were used as the control sample. As shown in Figures 7a–7c, the contact angle of CCS distinctly reduces from 65.5° to 23.5° after the coating of ceramic particles, and the contact angle of CCS@PFR further decreased to 19.4°. This result shows that the PFR modification can further improve the affinity of CCS membrane to electrolyte, which is attributed to that the hydroxyl group of the PFR validly increases the polarity of the separator, thereby improves the affinity of the separator with the polar electrolyte. What's more, the Al_2O_3 only improves the affinity of coating layer, while the PFR can penetrate through entire substrate separator to improve the overall wettability of membrane. As shown in Figure S6, the contact angle of the PE side of CCS@PFR reduces from 65.5° to 45.2°, which also demonstrates that the PFR can actually improve the affinity to electrolyte.

Several essential parameters of separators are list in Table I.The thickness of separator has no an obvious increase after the modification of PFR, which is consistent with the SEM result of the cross-section morphology of the membrane. As a result, it is beneficial to keep the high energy density of batteries. The porosity of CCS@PFR has a little reduction from 47.8% to 45.3% compared with CCS, while is slightly larger than PE separator, which is owing to the neutralization of the increase from ceramic layer and the decrease from the modification of PFR in the pores of PE substrate separator. Compared to the original CCS membrane, the electrolyte uptake of CCS@PFR declines from 82% to 73%, which is in accordance with the result of reduction of porosity due to the PFR modification. In spit of this, the electrolyte uptake of CCS@PFR is still much larger than PE since the excellent interfacial compatibility promoted the CCS@PFR to absorb more electrolyte. As is well known, the ionic conductivity mainly relies on the uptake amounts of liquid electrolyte in the separators. As a result, the ionic conductivity of CCS@PFR slightly deceases from 0.67 $mS\cdot cm^{-1}$ to 0.62 $mS\cdot cm^{-1}$ compared to CCS, while is rather larger than the 0.54 $mS\cdot cm^{-1}$ of PE, calculated using Equation 4, where the R_b is got by fitting the Nyquist plots with the equivalent circuit model inset in Figure 7d. And the fitting results of PE, CCS and CCS@PFR are 1.86 Ω, 1.72 Ω, 1.84 Ω, respectively, as shown in the enlarged profiles of the fitting plots inserted in Figure 7d too.

Table I. Physical properties of PE, CCS and CCS@PFR.

Separator	PE	CCS	CCS@PFR
Thickness (μm)	20	23	23
Porosity (%)	44.2	47.8	45.3
Contact angle (°)	65.5	23.5	19.4
Electrolyte uptake (%)	56	82	73
Ion conductivity ($mS\cdot cm^{-1}$)	0.54	0.67	0.62

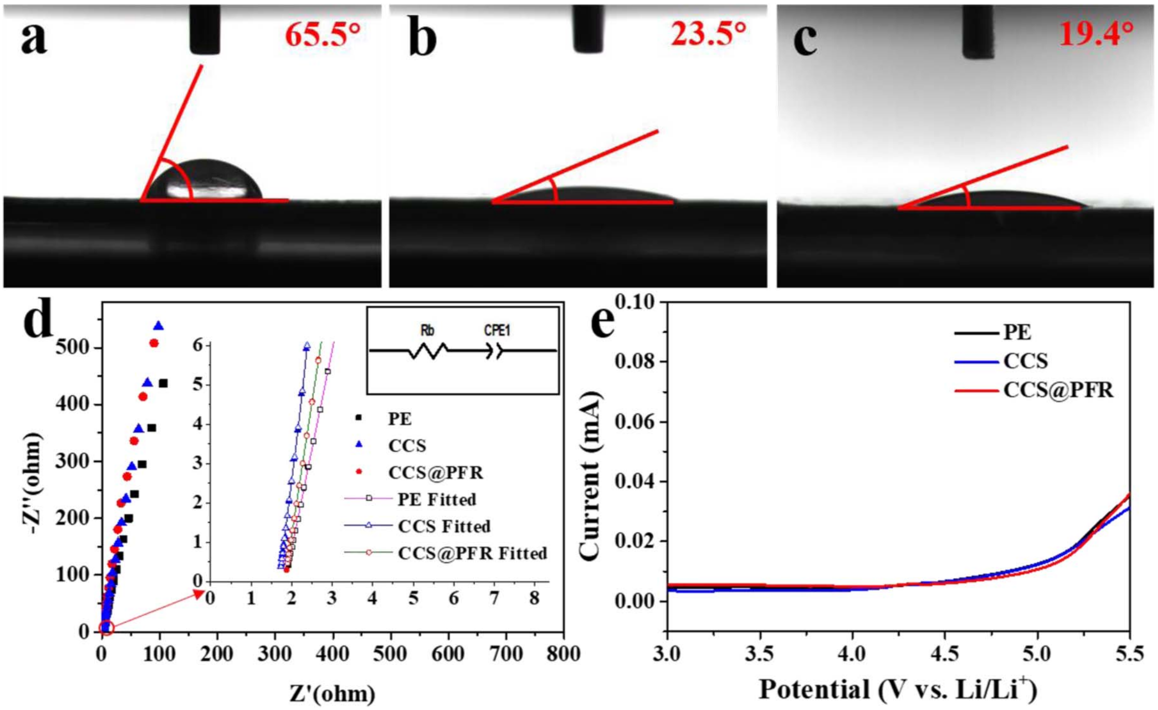

Figure 7. Contact angle images: (a) PE, (b) ceramic coating side of CCS, (c) ceramic coating side of CCS@PFR, (d) electrochemical impedance spectroscopy of PE, CCS and CCS@PFR, (The insets show the equivalent circuit and the enlarged profiles, which were involved to fit and calculate the ion conductivities) (e) LSV of PE, CCS and CCS@PFR at the rate of 1 mV·s^{-1}.

Electrochemical performance.—The electrochemical stability is a basic requirement of separators to ensure the high-performance of LIBs within it's working voltage. The electrochemical stability of the separators was evaluated by LSV at the rate of 1 mV. s^{-1} from 3 V to 5.5 V (vs Li/Li$^+$). As shown in Figure 7e, both the CCS and CCS@PFR have almost the same electrochemical stability as PE separator, the oxidation current of all the three kinds of separators began to increase at around 4.5 V, demonstrating that the coating of PFR will not influence the electrochemical stability of pristine membrane. Both the CCS and CCS@PFR can meet the requirement of most commercial cathode materials.

Furthermore, The battery cycling performance with different separators has been investigated by the Li/LiNi$_{0.6}$Co$_{0.2}$Mn$_{0.2}$O$_2$ coin-type half-cells at the current of 0.5 C with potential ranging from 3.0 V to 4.3 V. Figure 8a shows the discharge capacity and coulombic efficiency of the cells with PE, CCS and CCS@PFR. After 100 cycles, the cells with the PE, CCS and CCS@PFR separator maintain 86.7%, 87.5% and 87.6% of their initial capacity, respectively, and the coulombic efficiency of all the three kinds of separators remained above 99%. In addition, the charge/discharge curves of the cell assembled with CCS@PFR at different cycles are provided in Figure 8b, which is the same as the typical charge/discharge curves of the LiNi$_{0.6}$Co$_{0.2}$Mn$_{0.2}$O$_2$ anode. So that, the cycling performance indicates that the further modification of CCS membrane with PFR has no negative impact on the cycling performance of cell.

The rate capability of the PE, CCS and CCS@PFR has been tested at the rates of 0.5 C, 1 C, 2 C, 5 C, 10 C for 5 cycles and finally back to 0.5 C. As shown in Figure 8c, the discharge capacity of the cell with PE dropped drastically, with the increase of the current rate, only retaining 87.5%, 77.6%, 55.2% at the rate of 2 C, 5 C, 10 C respectively. By contrast, both the CCS and CCS@PFR exhibited an improved capacity retention, retaining 91.3%, 91.4% at the rate of 2 C, and 84.2%, 82.9% at the rate of 5 C, respectively. This is because the surface of CCS and CCS@PFR has a better wettability with electrolyte, which facilitates the transport of lithium ion in the electrolyte. However, compared to the cells assembled with CCS, the rate capacities of batteries assembled with CCS@PFR reveal a little decrease at 10 C, which is owing to the coating of PFR slightly reduces the porosity and the ionic conductivity of CCS, such that the ionic conductivities may not meet the need of cell at a higher rate. Even so, a higher porosity PE separator can be used as the base membrane to eliminate this effect and ensure the good power performance of LIBs for practical application.

To further explain the improvement of rate capacity, the charge/discharge curves of the cells assembled with CCS@PFR and PE separators at different rates are shown in Figure 8d. As it shown, the charge/discharge curves of PE and CCS@PFR are almost the same at relatively low rates of 0.5 C and 1 C. However, the polarization voltage of the cell assembled with PE separator increases dramatically, with the rise of the current rate. By contrast, the CCS@PFR has a slighter polarization voltage as the increase of current rate. The reason can be elucidated as follows: the rate capacity of LIBs is affected by the transfer of lithium ion in electrolyte, the electrode conductivity of electrodes (ECE), and the electrochemical reaction on the solid-liquid interface (ERSLI). At relatively low rates, the ionic conductivities is high enough to support the ECE and ERSLI, and the ECE and ERSLI act as the rate determining factors, so that the rate capacity of the cells assembled with PE separator and CCS@PFR display a similar discharge capacity at relatively low rates. However, at a higher rate, the ionic conductivities could not fully meet the requirement of the ECE and ERSLI. The lower the ionic conductivity is, the larger the concentration polarization will be. Therefore, the cell assembled with PE separator suffers from a larger polarization, and the better wettability of the CCS@PFR, which facilitates the transport of lithium ion in the electrolyte, promises a better rate performance, compared to PE separator.

Conclusions

In summary, the CCS@PFR has been successfully prepared via a simple soakage process, and a PFR three-dimension coating layer was formed throughout the entire CCS membrane. The three-dimension

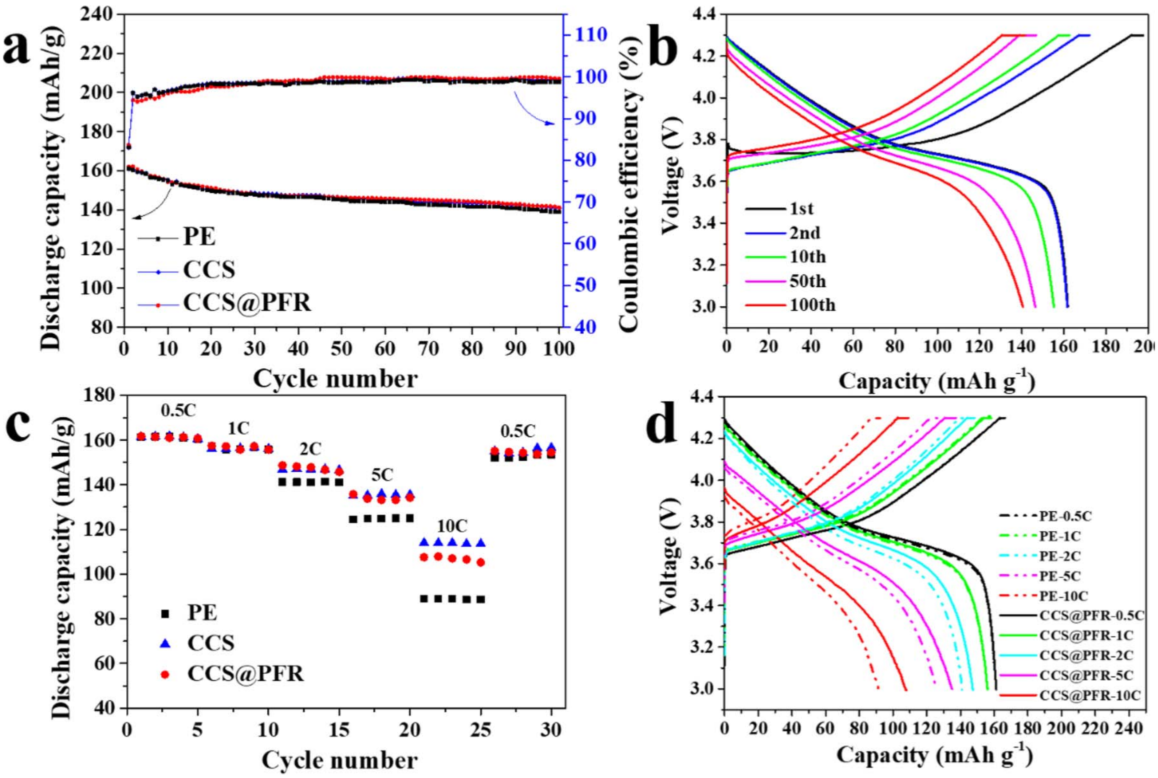

Figure 8. (a) The cycle performance of Li/LiNi$_{0.6}$Co$_{0.2}$Mn$_{0.2}$O$_2$ coin cell assembled with PE, CCS and CCS@PFR at the rate of 0.5 C, (b) the charge/discharge curves of the cell assembled with CCS@PFR at different cycles, (c) the rate capability of the Li/LiNi$_{0.6}$Co$_{0.2}$Mn$_{0.2}$O$_2$ coin cells assembled with PE, CCS and CCS@PFR. (d) the charge/discharge curves of the cells assembled with PE separator and CCS@PFR at different rates.

coating layer connects the ceramic layer with the PE layer as a whole, which not only enhances the mechanical strength of ceramic layer, preventing it from crashing with the shrinking of the polyolefin membrane, but also improves the adhesion between the ceramic layer and polyolefin separator, averting the exfoliation of ceramic layer. The thermal shrinkage tests verify that the CCS@PFR separators have extremely high thermal dimensional stability without visible thermal shrinkage even up to 300°C. The stretching strength of the separators after a heat-treatment also shows that the CCS@PFR maintains a high mechanical strength after a heat-treatment of 220°C. The cells assembled with the CCS@PFR show a shutdown function, which can significantly prevent the batteries from further thermal runaway at high temperatures. With the advantages of abundant sources, low cost, simple preparation process and environment-friendly property, the CCS@PFR separator can be expected to replace the commercial ceramic-coated separators, and greatly improve the safety of the LIBs, as well as easily accomplish the application of LIBs in power batteries and large-scale energy storage devices.

Acknowledgments

We gratefully acknowledge the financial support from the National Natural Science Foundation of China [grant Numbers 21503180, 21273185, 21621091], the Fundamental Research Funds for the Central Universities [grant Number 20720170037], and the National Key Research and Development Program of China [grant Number 2017YFB0102000]. The authors also wish to express their thanks to Dr. Daiwei Liao of Xiamen University for his valuable suggestions.

ORCID

Jinbao Zhao https://orcid.org/0000-0002-2753-7508

References

1. T. H. Kim, J. S. Park, S. K. Chang, S. Choi, J. H. Ryu, and H. K. Song, *Adv. Energy Mater*, **2**, 860 (2012).
2. J. Hassoun, S. Panero, P. Reale, and B. Scrosati, *Adv Mater*, **21**, 4807 (2009).
3. H. S. Jeong, D. W. Kim, Y. U. Jeong, and S. Y. Lee, *J. Power Sources*, **195**, 6116 (2010).
4. K. W. Song and C. K. Kim, *J. Membrane Sci*, **352**, 239 (2010).
5. J. A. Choi, S. H. Kim, and D. W. Kim, *J. Power Sources*, **195**, 6192 (2010).
6. X. S. Huang and J. Hitt, *J. Membrane Sci*, **425**, 163 (2013).
7. D. Takemura, S. Aihara, K. Hamano, M. Kise, T. Nishimura, H. Urushibata, and H. Yoshiyasu, *J. Power Sources*, **146**, 779 (2005).
8. R. l'Abee, F. DaRosa, M. J. Armstrong, M. M. Hantel, and D. Mourzagh, *J. Power Sources*, **345**, 202 (2017).
9. D. Li, D. Shi, Z. Yuan, K. Feng, H. Zhang, and X. Li, *J. Membrane Sci*, **542**, 1 (2017).
10. H.-J. Ha, E.-H. Kil, Y. H. Kwon, J. Y. Kim, C. K. Lee, and S.-Y. Lee, *Energy Environ. Sci*, **5**, 6491 (2012).
11. W. Zhang, J. Nie, F. Li, Z. L. Wang, and C. Sun, *Nano Energy*, **45**, 413 (2018).
12. Y. Liu, C. Li, B. Li, H. Song, Z. Cheng, M. Chen, P. He, and H. Zhou, *Adv. Energy Mater*, 1702374 (2018).
13. J. Zhang, J. Zhao, L. Yue, Q. Wang, J. Chai, Z. Liu, X. Zhou, H. Li, Y. Guo, G. Cui, and L. Chen, *Adv. Energy Mater*, **5**, 1501082 (2015).
14. P. Yang, P. Zhang, C. Shi, L. Chen, J. Dai, and J. Zhao, *J. Membrane Sci*, **474**, 148 (2015).
15. P. Zhang, L. Chen, C. Shi, P. Yang, and J. Zhao, *J. Power Sources*, **284**, 10 (2015).
16. C. Shi, P. Zhang, L. Chen, P. Yang, and J. Zhao, *J. Power Sources*, **270**, 547 (2014).
17. C. Shi, J. Dai, C. Li, X. Shen, L. Peng, P. Zhang, D. Wu, D. Sun, and J. Zhao, *Polymers*, **9**, 159 (2017).
18. C. Shi, J. Dai, X. Shen, L. Peng, C. Li, X. Wang, P. Zhang, and J. Zhao, *J. Membrane Sci*, **517**, 91 (2016).
19. J. A. K. R. A. Follensbee, A. W. Christiansen, G. E. Myers, and R. L. Gelmer, *J. Appl. Polym. Sci*, **47**, 1481 (1993).
20. Z. L. Yu, N. Yang, V. Apostolopoulou-Kalkavoura, B. Qin, Z. Y. Ma, W. Y. Xing, C. Qiao, L. Bergstrom, M. Antonietti, and S. H. Yu, *Angew. Chem., Int. Ed*, **57**, 4538 (2018).
21. J. Wang and Y.-F. Zhang, *Polym-Plast. Technol*, **51**, 1213 (2012).
22. S. Sachdeva and A. Kumar, *J. Membrane Sci*, **329**, 2 (2009).
23. A. Tejado, C. Pena, J. Labidi, J. M. Echeverria, and I. Mondragon, *Bioresour Technol*, **98**, 1655 (2007).
24. Q. Feng, M. Yao, Z. Su, and X. Yao, *Ceram. Int*, **44**, 11160 (2018).
25. D. L. Kun Yang and Baoshan Xing, *Langmuir*, **25**, 3571 (2009).
26. X. Zhang, E. Sahraei, and K. Wang, *Sci Rep*, **6**, 32578 (2016).

27. P. G. Balakrishnan, R. Ramesh, and T. Prem Kumar, *J. Power Sources*, **155**, 401 (2006).
28. J. Dai, C. Shi, C. Li, X. Shen, L. Peng, D. Wu, D. Sun, P. Zhang, and J. Zhao, *Energy Environ. Sci*, **9**, 3252 (2016).
29. D. Wu, C. Shi, S. Huang, X. Qiu, H. Wang, Z. Zhan, P. Zhang, J. Zhao, D. Sun, and L. Lin, *Electrochimica Acta*, **176**, 727 (2015).
30. L. Kong, B. Liu, J. Ding, X. Yan, G. Tian, S. Qi, and D. Wu, *J. Membrane Sci*, **549**, 244 (2018).